Applied Thermal Engineering 275 (2025) 126808

Contents lists available at ScienceDirect

Applied Thermal Engineering

journal homepage: www.elsevier.com/locate/apthermeng

Research Paper

An experimental investigation of indirect evaporative cooling in gyroid-based heat exchangers

Nicolò Morselli *, Marco Puglia, Michele Cossu, Simone Pedrazzi, Alberto Muscio, Paolo Tartarini, Giulio Allesina

Department of Engineering "Enzo Ferrari", University of Modena and Reggio Emilia, Via Vivarelli 10/1, 41125 Modena, Italy

ARTICLE INFO

Keywords:
Triply periodic minimal surfaces
Gyroid
3D printing
Heat exchangers
Indirect evaporative cooling (IEC)

ABSTRACT

This study explores the performance of crossflow indirect evaporative coolers (IECs) based on gyroid geometries and fabricated using PLA through fused filament fabrication. Different gyroid cell sizes were tested in both dry and wet conditions. Dry tests demonstrate high heat transfer performance, with a maximum convective heat transfer coefficient of approximately 170 W/(m^{2}K) in turbulent flow. Under wet conditions, the gyroid-based IECs achieved a volumetric cooling capacity three times higher than traditional crossflow heat exchangers, while the wet-bulb efficiency reached up to 90 %, highlighting the benefits of high surface-to-volume ratios for enhanced evaporation. Although the coefficient of performance (COP) of gyroid-based IEC peaked between 57.9 and 84.7 in high temperature and low humidity conditions, conventional IEC reach values 2–5 times higher under milder operating conditions, typical of temperate climates with moderate humidity, due to lower pressure drop. In any case, the COP remains significantly superior to that of vapor compression cooling systems. A key limitation of this study is the scale of the tested prototypes, which may not fully capture performance and distribution challenges in larger systems. However, although the results are not directly scalable, they provide a consistent comparison of the performance of different geometries suggesting that gyroid-based IECs are particularly suitable for cooling applications requiring compactness and high-power density.

1. Introduction

Climate change and the continuous increase in extreme weather events, such as persistent heat waves, bring to the forefront the issue of cooling inhabited spaces. It is well known that heating demand is decreasing across the European domain, while the opposite is happening for cooling demand [1], where the constant improvement in socio-economic conditions in many countries, has also led to an exponential growth in the spread of air conditioning systems. The 2023 IEA report [2] estimates that energy consumption for space cooling will more than double by 2050 if no action is taken. Looking back at data from previous reports [3], energy consumption for space cooling has more than tripled since 1990, accounting for about 16 % of total electricity consumption in the building sector in 2021 (2 GWh). This trend has led to immediately measurable effects, such as an increase in power outages [4], as well as an estimated rise in global CO_2-equivalent emissions, from 566 to 994 $MtCO_2$. This constant growth scenario in energy consumption and greenhouse gas emissions has prompted the European Green Deal [5], which aims for a net reduction of 55 % in greenhouse gas emissions by 2030 compared to 1990 levels, and carbon neutrality by 2050. To achieve these goals, it is estimated that emission intensity (average CO_2 emissions per unit of cooling) will need to be reduced by about two-thirds, driving research toward new cooling systems.

As long as air conditioning systems currently installed are primarily based on vapor compression refrigeration (VCR), which use refrigerants (such as R134A, R22, etc.) to remove heat from the cooled environment. Due to the required compression of the refrigerant fluid, this process is characterized by high electricity consumption and, although there have been significant advancements in recent years, the coefficient of performance (COP) ranges, on average, between 2 and 5 [6]. Additionally, it should not be overlooked that the use of some of the above-mentioned refrigerants remains one of the main contributors to the greenhouse effect [7].

If air conditioning becomes necessary due to prolonged heatwaves or health concerns, systems should be efficient and equitably accessible, and a sustainable cooling strategy should develop low-energy cooling systems for future climates [3]. In this context, evaporative cooling

* Corresponding author.
E-mail address: nicolo.morselli@unimore.it (N. Morselli).

https://doi.org/10.1016/j.applthermaleng.2025.126808
Received 17 December 2024; Received in revised form 8 May 2025; Accepted 10 May 2025
Available online 12 May 2025

Nomenclature

Parameter	Description(Unit
A	Heat transfer surface area m^2
COP	Coefficient of performance –
CSA	Cross-sectional area m^2
D_H	Hydraulic diameter m
f	Fanning friction factor –
h	Convective heat transfer coefficient $\frac{W}{m^2K}$
$\dot{m}$	Mass flow rate $\frac{kg}{s}$
Nu	Nusselt number –
Δp	Pressure drop Pa
Pr	Prandtl number –
$\dot{Q}$	Heat transfer rate W
$\dot{Q}_{cool}$	Cooling capacity W
Re	Reynolds number –
ΔT_{LM}	Logarithmic mean temperature difference $^\circ C$
$\dot{W}_{el}$	Electrical power W
$\dot{W}_p$	Pumping power W

Greek Letters	Description
η	Efficiency –
λ_{PLA}	Thermal conductivity of PLA material $\frac{W}{mK}$
μ	Dynamic viscosity $Pa{\cdot}s$
ρ	Density $\frac{kg}{m^3}$
ω	Absolute humidity $\frac{g_{vap}}{kg_{da}}$

Acronyms	Description
FFF	Fused Filament Fabrication
HX	Heat exchanger
IEC	Indirect evaporative cooling
PLA	Polylactic acid
TPMS	Triply Periodic Minimal Surface

Subscripts	Description
$1, 2, 3, 4$	Air channels (specific to the test rig configuration)
amb	Ambient
da	Dry air
DB	Dry bulb
fan	Fan-related terms
vap	Vapor
WB	Wet bulb

architectures, which exploit the latent heat of water evaporation to remove sensible heat from an air stream, find their niche. These systems are mainly divided into two categories: direct evaporative coolers (DEC) and indirect evaporative coolers (IEC).

In DEC, water is evaporated within the same airflow used for cooling the target environment. This technology often employs porous panels made of different materials (a comprehensive review of materials used is reported in [8]), which are continuously kept wet. The advantage is a high wet bulb efficiency, reported in Eq. (1), which represents the ability of DEC to approach the physical limit of the incoming wet bulb temperature [9]. The main drawback is the increase in relative humidity of the cooled environment, which can negatively affect occupant comfort in most of the climatic conditions. Moreover, the potential emergence of *Legionella*, due to the presence of droplets in the supply air flow [10] underscores the importance of stringent control measures. For this reason, DEC solutions are more commonly used in agriculture, industry or arid climates.

IEC, in their simplest form, consist of two channels separated by a heat transfer surface. In the wet channel, working air is circulated while water is sprayed onto the surface facilitating the heat transfer. Water evaporation is sustained harvesting heat from: the surrounding air itself, the septum separating the channels and, consequently, the dry channel where the product air is cooled before being delivered to the target space. The moist working air is then exhausted into the atmosphere, never coming into contact with the cooled environment, leading to the limitations of the drawbacks previously mentioned. However, the presence of a heat transfer surface introduces a chain of thermal resistances that reduce the system's overall efficiency. Moreover, the operating regime of IECs can depend on the type of application, e.g. in data centers' cooling, where the IEC can conveniently operate in recirculation mode: the exhaust product air is extracted from the datacenter and then returned to the indoor environment after being cooled by the IEC unit [11]. This solution decouples the inlet temperature and humidity conditions of the dry and wet channels. In buildings, however, IECs are commonly adopted not only for cooling but also to provide fresh air exchange, and the two IEC channels can therefore operate with identical inlet air temperature and humidity, corresponding to the external environment condition.

For IEC systems, the wet bulb efficiency (η_{wb}) is an indicator of how closely the HX approaches the physical limit of the wet bulb temperature measured at the wet channel inlet [9] as reported in Eq. (2) and typically ranging between 40 % and 60 % [12], compared to 70 %-95 % for DEC systems [8].

$$\eta_{wb,DEC} = \frac{T_{air,i} - T_{air,o}}{T_{air,i} - T^{wb}_{air,i}} \tag{1}$$

$$\eta_{wb,IEC} = \frac{T_{p,i} - T_{p,o}}{T_{p,i} - T^{wb}_{w,i}} \tag{2}$$

Despite the reduced performance compared to DEC systems, IECs can benefit from COP 5–6 times greater than VCR systems [13]. Nevertheless, their performance is strongly dependent on ambient temperature and humidity and, in high wet bulb temperature conditions, the product air temperature may not meet thermal comfort requirements.

There are examples of tubular IECs, counter-crossflow IECs, and heat pipe-based IECs, but the most common architectures are typically counter-flow and crossflow [14]. In the former (as shown in Fig. 1a), the product and working airflows pass through separate channels in

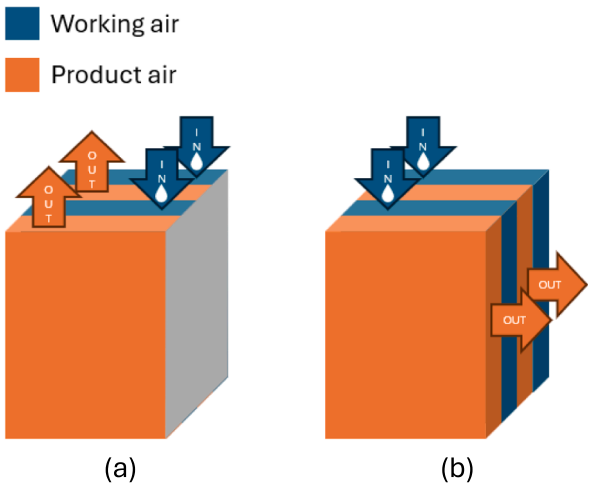

Fig. 1. Schematic of a counter-flow IEC (a) and cross-flow IEC (b) architectures.

opposite directions, while in the latter (Fig. 1b), the flows are orthogonal to each other in separate channels. Water is usually pumped and sprayed through nozzles onto the wet surfaces exposed to the working air. Some commercial systems also use overflow water distribution systems, reducing the risk of nozzle clogging [15].

Currently, research on IEC systems focuses on improving water distribution and water-surface interaction inside the HX. Topics that are actively being studied are the use of new porous materials (such as fibres, zeolites, and ceramics) for coating the HX surfaces [16] and air flow and nozzles arrangement for optimal humidification [17]. Additional research has tested different heat exchange surface geometries with positive effects on wettability, leading to improved IEC performance [11]. These advances have resulted in COP for the IEC higher than 30 and η_{wb} exceeding 90 % [18].

As described later in this introduction, strong drivers pushing towards the use of polymeric materials in IEC can be found in literature.

In fact, despite examples of polymeric materials used for IEC heat transfer surfaces are rare, some instances demonstrate COP values exceeding 8, with advantages in terms of corrosion resistance and fouling reduction [19]. Some examples of plastic-plate IECs can be found in the work of Chen et al. [20]. Despite this, current research largely prefer metallic materials (often aluminium alloys) for IEC construction due to their high thermal conductivity and ease of fabrication through a series of stacked parallel planar channels. Increasing the heat transfer surface area is primarily achieved by maximizing the number of channels within the unit volume, optimizing both effectiveness and fluid dynamic losses.

Following this approach, in recent years additive manufacturing (AM) has enabled the creation of complex geometries that are impossible to achieve with traditional methods, allowing for topological optimization of available space to maximize the heat transfer surface area for compact HXs [21]. Several AM technologies are available, allowing to produce both polymeric and metallic parts. Common polymer-based technologies include fused filament fabrication (FFF) and stereolithography (SLA). FFF involves the melting of a plastic filament to create successive horizontal layers of material [22], while SLA uses a laser to cure liquid resin into solid layers [23], typically resulting in more detailed and precise models compared to FFF. Metal parts are primarily produced using selective laser melting (SLM) technology [24].

Among the most promising geometries for HX design are Triply Periodic Minimal Surfaces (TPMS). TPMS are a class of implicit surfaces with three-dimensional periodicity, zero mean curvature, and a high surface-to-volume ratio. These structures can be precisely described by mathematical functions, allowing direct control over parameters such as porosity (the ratio of void to solid volume) and specific surface area [25]. When properly plugged, TPMS can divide space into two distinct volumes connected through a single, continuous heat transfer surface, enabling the easy creation of crossflow HXs. A complete description of the equations governing the available TPMS is provided in the work by Reynolds et al. [26].

The interest in TPMS-based HXs is high, as these surfaces tend to promote an earlier transition to turbulent flow regimes compared to traditional geometries, although the exact point of transition is still not univocally defined [26,27]. This flow transition characteristic, coupled with their high surface-to-volume ratio, offers the potential to significantly enhance the heat transfer compared to the traditional high-performance HX designs [21].

In this regard, several studies have investigated the thermo-fluid-dynamic behaviour of TPMS-based crossflow HX, both numerically and experimentally, analysing both metal-based and polymer-based lattices [28]. The most significant studies on this topic are summarized below to provide an overview of the available literature.

Dixit et al. characterized a hybrid experimental/numerical 32×32×32 mm liquid–liquid crossflow HX based on gyroid-type TPMS, the structure identified by Alan Schoen in 1970 [29], particularly suitable for the purpose as it belongs to the TPMS with cubic symmetry. Dixit et al. achieved a surface area-to-volume ratio of 670 m^2/m^3 and a specific weight of 240 kg/m^3, with an heat transfer effectiveness increase of 55 % and a tenfold reduction in size compared to a standard counter-flow HX. The authors show an overall heat transfer coefficient of 120–160 W/mˆ2 °C in the *Re* range of 15 to 40 [21].

Reynolds et al. run experiments on several TPMS geometries by creating cross-flow water–air HXs and analysing the film heat transfer coefficient over a wide range of Re numbers (100–2500), asserting that the use of gyroid-based TPMS is the best performer and can increase *Nu* by 112 % compared to a geometry with circular tubes arranged in the same volume. The thermo-hydraulic efficiency comparison shows that, for the same pumping power, the Nu is 13 % higher than in a straight-tube HX, further demonstrating the potential of gyroids for HX miniaturization [26].

Yan et al. numerically studied various TPMS structures, demonstrating a 90–110 % increase in the performance evaluation coefficient (PEC) compared to a crossflow parallel channel structure, showing that the diamond-type TPMS structure has the highest volumetric performance, while the gyroid has the best performance in terms of HX weight. The study investigates a Re range between 200 and 500 showing that TPMS HXs function as "*3D homogeneous mixing flow HXs*" thanks to the continuous merging and splitting of the fluid flow that enhances the heat transfer by constantly interrupting the boundary layer [30].

Iyer et al. conducted an exclusively numerical study on the performance of TPMS-based geometries in a Re range of 10 to 400, calculating that the best performance is provided by the Schwartz-D TPMS-based geometry, offering a reduction in footprint by over 90 % compared to a smooth tube HX operating under the same conditions [27].

Femmer et al. compared TPMS-based, flat-sheet and hollow-fibre architectures for membrane technology applications, through both numerical and experimental approaches. The prototypes were fabricated using 3D printing with liquid photo-polymerizable resin. The results, although limited to a Re range of $1 - 15$, showed a tenfold increase in heat transfer performance compared to a smooth tube operating under the same conditions [31].

Adding to this the study by Li et al. [32], which performed a CFD analysis of water/supercritical CO_2 TPMS-based HX extending the calculation to highly turbulent flow regimes ($7000 < Re < 55000$), highlighting that TPMS structures hold great potential for heat transfer applications, outperforming traditional HXs. Additionally, it is noted that studies on these HX often utilize polymeric prototypes due to their relative ease of fabrication using FFF or SLA.

It is clear from the literature that TPMS-based HXs attract significant interest due to their high surface-to-volume ratio and ability to promote early turbulence transition, which enhances heat transfer and enables HX size reduction. Both numerical and experimental studies highlight their superior thermo-hydraulic performance, but, surprisingly, there are no reported applications in the field of IEC, where their potential remains, to date, unexplored. This study pioneers the investigation of TPMS-based IEC systems by experimentally assessing their performance under wet conditions. The ease that uniformly patterned, highly symmetrical TPMS offer to create crossflow HXs, and the promising performance of dry TPMS-based HX, highlight the possibility of creating compact evaporative coolers that could be applied in fields where space or weight constraints are critical, unlike the current scenario, where IECs are predominantly used for building cooling.

In this work, three different air-to-air crossflow IECs based on gyroid lattices with different dimensions were created and experimentally tested. The gyroid structure is widely adopted in the studies mentioned above, due to its excellent balance between heat transfer effectiveness and flow resistance, making it ideal for comparison with the existing literature. The HXs were fabricated using PLA via FFF, and initial dry tests were conducted to validate the experimental setup, comparing results in terms of *Nu* and friction coefficient with the available literature. In the second part of the work, the HXs built on gyroids are used as indirect evaporators by wetting one channel while keeping the other

dry, with air passing through both channels. This setup allows for the measurement of key operating parameters of an IEC, such as cooling capacity, COP, and wet bulb efficiency, providing the first experimental data on the performance of TPMS-based IECs under wet conditions.

2. Materials and methods

2.1. Cross flow heat exchanger based on gyroid primitive

This work uses gyroid-based cross-flow HXs, whose periodic surface can be described by the equation $\cos z + \sin z \cos x = C$ [24], where C is a constant that defines the wall thickness and, consequently, the porosity. The function has been implemented in Matlab [33], generating three different base units with a wall thickness of 0.8 mm and dimensions[1] of 5.4, 7.9, and 10.4 mm (Fig. 2a shows the Gyr7.5 base unit). These base unit sizes were chosen to cover a representative range of hydraulic diameters while ensuring compatibility with the manufacturing constraints and resolution limits of the fabrication process. Base units were then repeated to form elementary gyroid cells named Gyr5, Gyr7.5, and Gyr10 (Fig. 2b), whose dimensions are reported in Table 1. The repetition of base units and the appropriate plugging of sections on the outer surfaces were achieved by importing the STL file into the FreeCAD environment [34], allowing the separation of the TPMS into two non-communicating volumes divided by a single continuous surface (Fig. 2c). This surface becomes the heat transfer surface when the TPMS functions as a HX, while the two volumes become two separate channels for the thermal exchange fluids to flow through. Corner supports were then added to proper sealing with the HX housing, which will be described in the following section.

Table 1 summarizes the geometrical dimensions of the different gyroid-based cross-flow HXs used, while Table 2 provides the list of relevant dimensions for data reduction.

The 3D model was then imported (Table 3) into the slicer software Simplify3D, which was used to program the Sharebot43 printer for manufacturing via FFF using PLA[2] as the feed material. A printing speed of 60 mm/s and vertical resolution of 0.15 mm were selected, and care was taken to ensure a double-layer wall between channels to prevent internal porosity.

2.2. Test rig and uncertainty analysis

The experimental apparatus has been specifically designed to accommodate various types of air-to-air crossflow HXs and Fig. 3 shows a P&ID diagram and a picture of the setup, which consists of a horizontal and a vertical duct, with the housing (TPMS in the figure) for the cross-flow HX installed at their intersection. A 3 cm thick layer of polyurethane foam insulation is applied around the TPMS housing and the adjacent ducts.

The test rig allows independent control of temperatures and volumetric flow rates of the air in both channels of the HX being tested. These two parameters are regulated by an Arduino UNO microcontroller, which controls the speed of FAN1 and FAN2 through MOSFETs for PWM amplification, while the inlets air temperatures are controlled through PID feedback using auxiliary PTC temperature sensors at positions 1 and 2 in Fig. 3. Two solid-state relays independently power the electric heaters (HTR1 and HTR2).

Each air volumetric flow rate can be varied from 0 to 30 m^3/h while the temperature can be varied from ambient up to a maximum of 50 °C. The ambient temperature and humidity conditions are monitored using a Testo 0636–9732 thermo-hygrometric probe connected via bluetooth to a Testo 440 datalogger.

The inlet and outlet air temperatures of the HX are measured using 1/10-DIN precision platinum resistance thermometer probes (model SE012 by Pico Technology) with a diameter of 4 mm, connected to the PT104 datalogger by Pico Technology and positioned at points 1 to 4 in Fig. 3.

The volumetric flow rates of the two air streams are measured using two vane anemometers: a Testo 417 in the horizontal channel, positioned at point A in Fig. 3, and an Extech HD300 positioned at point B, at the exit of the vertical channel. The diameter of the measuring head of the two anemometers is 100 mm and 72 mm respectively, and the duct of the test rig are designed to perfectly fit the anemometers. The inlet of the Testo 417 is preceded by a straightener to rectify the flow in a shorter space. For the inlet of the Extech HD300, a length of 10 diameters was kept from the last concentrated pressure loss to ensure a fully developed flow [35].

The pressure drop generated by the HX under test is measured through the Chauvin Arnoux CA 1550 micromanometer by recording the differential pressure between points 3 and 4 ($\Delta p = p_3 - p_4$).

The test bench can also work in "wet mode", where, in the vertical channel, water is sprayed so as to create an IEC. For this purpose, a gear pump (PMP in Fig. 3a) connected to Arduino is used to match the desired duty cycle. Water is pumped through a nozzle positioned below thermoresistance number 2, and excess water is collected and drained through a siphoned outlet pipe located near point 4.

To control and to assess the effectiveness of water evaporation, a second Testo thermo-hygrometric probe is added at point B in Fig. 3 during wet tests to monitor evaporation efficiency.

A leak test was performed on each HX by pumping water on one side and ensuring that no liquid leakage occurred on the other side.

As described above, all the HXs investigated in this work have been additive manufactured. FFF produced a geometry with a not-neglectable surface roughness, which is also a consequence of the printing orientation. The surface characteristics, together with an intrinsic variability of the wall thickness, forced to first characterize the gyroids in dry (no water injection) configurations. This first experimental campaign serves as comparison with existing literature on gyroids.

The uncertainty for each equation was estimated using the method suggested by Kline and McClintock [36], which is well-suited for single measurements without repetitions and has already been used by several authors, such as Qian et al. [37] in the experimental study of TPMS in copper and by Chu et al. [12] applying it to the study of indirect evaporative HXs. The method assumes that the value of the result R is a function of $(x_1, x_2, \cdots, x_n)$ independent variables (Eq. (3)) and that each variable is affected by an absolute uncertainty equal to $(\theta_1, \theta_2 \cdots, \theta_n)$. The propagated measurement uncertainty on the result is called θ_R and its value is calculated using Eq. (4).

$$\boldsymbol{R} = \boldsymbol{f}(\boldsymbol{x_1}, \boldsymbol{x_2}, \ldots, \boldsymbol{x_n}) \tag{3}$$

$$\theta_R = \left[\left(\frac{\partial R}{\partial x_1} \theta_1 \right)^2 + \left(\frac{\partial R}{\partial x_2} \theta_2 \right)^2 + \cdots + \left(\frac{\partial R}{\partial x_n} \theta_n \right)^2 \right]^{\frac{1}{2}} \tag{4}$$

2.3. Data reduction

2.3.1. Heat transfer evaluation in dry conditions

To characterize the created HXs and to compare their performance with the experimental studies currently available in literature, a preliminary campaign of "dry" tests has been conducted without injecting water into the secondary (vertical) channel. This brings the test conditions in line with similar cases already reported in other studies, which most of them are well summarized in the work of Reynolds et al. [26].

It becomes therefore essential to describe the problem through a

[1] The additional 0.4 mm per cell is determined by half the wall thickness, as the other half of the thickness is inside the cell itself.

[2] The PLA used has an RAL 9010 color, a diameter of 1.75 mm, and is manufactured by Sharebot IT. The printing temperature is 215°C, the melting point ranges from 140°C to 160°C, and the specific heat capacity is 1800 J/(kg °C).

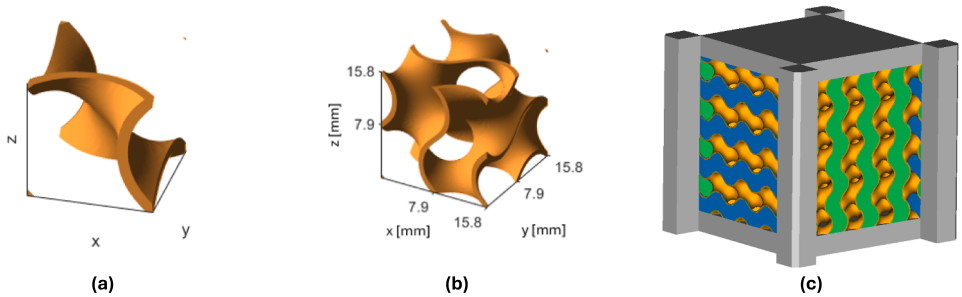

Fig. 2. Base unit of a gyroid (a), elementary cell of the Gyr7.5 structure (b) and the full HX modelled in FreeCAD (c) in which the TPMS closing structures necessary for the delimitation of the two separate volumes are highlighted in green and light blue.

Table 1
Geometrical parameter of the TPMS structures.

Name	Wall thickness (s) [mm]	Base unit length [mm]	Elementary cell length [mm]	Elementary cell repetition for the CFHX (x * y * z)	CFHX total length (L) in the flow direction [mm]	CFHX volume [dm^3]
Gyr5	0.8	5.4	10.8	6 * 6 * 7	0.0648 (60 cells)	0.317
Gyr7.5	0.8	7.9	15.8	4 * 4 * 4	0.0632 (40 cells)	0.252
Gyr10	0.8	10.4	20.8	3 * 3 * 3	0.0624 (30 cells)	0.243

Table 2
Uncertainty range of the instrument used.

Instrument	Resolution		Accuracy	
Thermo-anemometer Extech Instruments mod. HD300	0.01	$\frac{m}{s}$	$\pm 3\%_{mv}$	$\frac{m^3}{h}$
	0.1	$^{\circ}C$	± 2	$^{\circ}C$
Thermo-anemometer Testo mod. 417	0.01	$\frac{m}{s}$	$\pm(0.1+1.5\%_{mv})$	$\frac{m}{s}$
	0.1	$^{\circ}C$	± 0.5	$^{\circ}C$
Differential micromanometer Chauvin Arnoux CA 1550	0.1	Pa	$\pm(0.5\%_{mv}+1)$	Pa
Thermo-igrometer Testo 0636–9732 – calibrated Bluetooth connected	0.1	$\%_{RH}$	± 0.5	$\%_{RH}$
	0.1	$^{\circ}C$	± 0.5	$^{\circ}C$
Thermo-igrometer Testo 0636–9732 wire connected	0.1	$\%_{RH}$	± 2	$\%_{RH}$
	0.1	$^{\circ}C$	± 0.5	$^{\circ}C$
Platinum resistance thermometer Pico Technology mod. SE012	0.01	$^{\circ}C$	$\pm 0.03@0^{\circ}C \pm 0.07@50^{\circ}C$	$^{\circ}C$

dimensionless thermo-fluid dynamics perspective. In this context, characteristic numbers such as the *Re*, *Nu*, and the fluid dynamic Fanning friction factor (f) must be used.

Although the equivalent characteristic length of a gyroid is still a topic of ongoing discussion, *Re* is often defined by Eq. (5), where the reference length used is the hydraulic diameter of the TPMS (Eq. (6)), calculated as the ratio between the volume occupied by a single channel and the wetted surface area as suggested by Iyer et al. and Yan et al. [27,30]. It is also noted that the hydraulic diameter is averaged over the entire volume, while it constantly varies from section to section. Density and dynamic viscosity were calculated at the mean fluid temperature in each of the two regions of the exchanger, through interpolation from tables [35], while the average velocity (Eq. (7)) was determined as the mean volumetric flow rate divided by the average cross-sectional area defined in Eq. (8).

$$Re_H = \frac{\rho w D_H}{\mu} \tag{5}$$

$$D_H = \frac{4V_{channel}}{A} \tag{6}$$

$$w = \frac{\dot{V}}{CSA} \tag{7}$$

$$CSA = \frac{V_{channel}}{L} \tag{8}$$

Reynolds et al. work [26] suggests that in TPMS paths, the flow becomes turbulent at a *Re* as low as 150, implying that the dimensionless analysis of pressure losses can be framed by using the Fanning friction factor (f) for turbulent flows. It correlates the Δp across the HX to the dynamic pressure of the fluid $\frac{1}{2}\rho w^2$ through the geometrical dimensions D_H and L, as well described by Reay et al. [38] and defined in Eq. (9).

$$\frac{\Delta p}{L} = \frac{4}{D_H} f \frac{1}{2}\rho w^2 \rightarrow f = \frac{\Delta p D_H}{2\rho w^2 L} \tag{9}$$

To evaluate heat transfer, we combined a first-principle energy balance on the individual channel (Eq. (10)) with the use of the logarithmic mean temperature difference equation (Equation (11)) (ΔT_{LM}), which allows the calculation of the overall heat transfer coefficient U through the measurement of the sensible heat transfer rate ($\dot{Q}$), the heat transfer surface area A, and the correction factor F. Commonly available relationships for counter-flow HX were then corrected and used [35].

$$\dot{Q} = \dot{m} c_p (T_{out} - T_{in}) \tag{10}$$

$$\dot{Q} = UAF\Delta T_{LM} \tag{11}$$

Gyroid HX is divided into two convoluted volumes, separated by a sin-

Table 3
Relevant parameters for thermo-fluid-dynamic calculation.

Type	Heat transfer surface area (A) [mm^2]	Cross section area (CSA) [mm^2]	D_H [mm]
Gyr5	91,860	2248	6.1
Gyr7.5	51,750	1898	8.5
Gyr10	36,560	1870	12.6

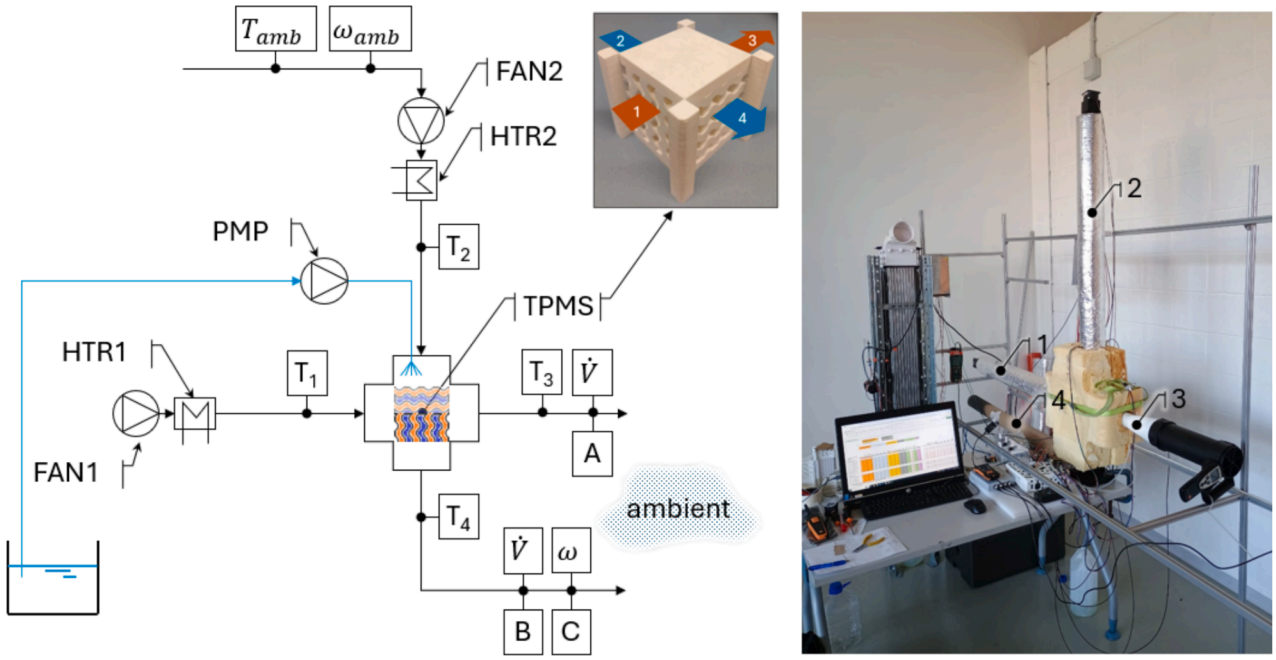

Fig. 3. Schematic of the test rig and photographs of the Gyr7.5 HX with a representation of the two separate cross flows and of the experimental apparatus.

gle, continuous heat transfer surface with area A, thickness s, and thermal conductivity λ_{PLA}.

The overall thermal resistance is therefore the result of three contributions: the convective thermal resistance of channel 1–3, the conductive thermal resistance of the separating wall, and the convective thermal resistance of channel 2–4. These combine to define the overall heat transfer coefficient U as indicated in Eq. (12).

In this equation, the heat transfer surface area is assumed to be $A = \frac{A_{13}+A_{24}}{2}$, since the thin wall thickness makes the surfaces of channel 1–3 and channel 2–4 very similar to each other.

$$\frac{1}{UA} = \frac{1}{h_{13}A} + \frac{s}{\lambda_{PLA}A} + \frac{1}{h_{24}A} \tag{12}$$

To determine the convective heat transfer coefficient and subsequently to derive the Nu, it is necessary to know one of the two thermal resistances due to convection. In the work of Reynolds et al. [26], since the HX involved air and water, it was reasonable to assume that the thermal resistance on the water side due to convection was negligible or very small in comparison to the air side one. In other studies, the wall temperature was evaluated using CFD models [21,39] and then the Newton's law of convection was applied.

In this work, dry experiments were conducted to maintain flow conditions as identical as possible between channels 1–3 and 2–4, allowing for the assumption $h_{13} \approx h_{24} = h$ and enabling the calculation of a mean convective coefficient that is similar for both channels. The procedure, also adopted by Femmer et al [31], is presented in Eq. (13), where U is determined experimentally by measuring $\dot{Q}$ and ΔT_{LM}.

$$\frac{1}{UA} \approx \frac{1}{hA} + \frac{s}{\lambda A} + \frac{1}{hA} \rightarrow h \approx \frac{2}{\frac{1}{U} - \frac{s}{\lambda_{PLA}}} \tag{13}$$

$$Nu_H = \frac{hD_H}{\lambda_{air}} \tag{14}$$

Nu can thus be derived from the relationship reported in Eq. (14), which relates to the λ_{air}, averaged over the inlet and outlet conditions of the fluid using values available from tables [35].

In the results section, these relationships are used to contextualize the results obtained with the tested heat transfer devices in relation to literature. The main thermofluid dynamic parameters analyzed previously are summarized in the table.

The experimental campaign involved tests at different air inlet temperatures for channel 1–3, while maintaining a constant air inlet temperature for channel 2–4. The air flow rate was also varied for both channel 1–3 and channel 2–4 to properly evaluate Nu number under symmetric conditions for the two channels. The values were averaged over a 2-minute period after allowing sufficient time for the system to reach steady-state conditions.

Table 4 summarizes the test conditions for the different HXs, where the maximum Re achievable was dependent on the pressure drop for each geometry.

2.3.2. Heat transfer evaluation in wet conditions

When water is injected into channel 2–4, the gyroid-based HX operates as an indirect evaporative cooler. In channel 2–4, a direct evaporative cooling process occurs, which absorbs heat from channel 1–3 through the evaporation of water.

Indirect evaporative coolers are evaluated based on their performance in terms of cooling capacity ($\dot{Q}_{cool}$) and COP [40], which respectively represent the thermal power removed from the working air to the product air (from 2 to 4 to 1–3) and the efficiency of using primary energy to achieve heat transfer, as outlined in Eqs. (15) and (16).

In calculating the COP, the mechanical power drawn for pumping water in channel 2–4 was not considered, as the pump used is oversized for the requirements.

$$\dot{Q}_{cool} = \dot{m}c_p(T_3 - T_1) \tag{15}$$

$$COP = \frac{\dot{Q}_{cool}}{\dot{W}_{el}} \text{ where } \dot{W}_{el} = \frac{\dot{W}_{p,13} + \dot{W}_{p,24}}{\eta_{fan}} \text{ and } \dot{W}_p = \dot{V}\Delta p$$

Table 4
Tests under dry conditions.

TPMS	T_1[°C]	T_2[°C]	Re
Gyr10	25 –50	25	785 –2906
Gyr7.5	25 –50	25	523 –1740
Gyr5	25 –50	25	376 –976

IEC performances are heavily dependent on the ability of the wet channel to evaporate water. Since we are dealing with cross-flow IEC, this capability is represented by $\eta_{wb,IEC}$, that is now framed into our nomenclature simply as η_{wb} reported in Eq. (17) [40].

$$\eta_{wb} = \frac{T_1 - T_3}{T_1 - T_{2,wb}} \tag{17}$$

For the calculation of $T_{2,wb}$ the Stull equation, reported in Eq. (18) was used. This equation provide a good interpolation from −20 °C to 50 °C and for $RH_{\%}$ between 5 and 99 % with mean absolute error of less than 0.3 °C [41].

$$T_{wb} = T_{db}\cdot atan[0.151977(RH_{\%} + 8.313659)^{\frac{1}{2}}] + atan(T_{db} + RH_{\%}) - atan(RH_{\%} - 1.676331) + 0.00391838(RH_{\%})^{\frac{3}{2}}\cdot atan(0.023101RH_{\%}) - 4.686035 \tag{18}$$

The performance parameters depend also on the inlet temperature and humidity conditions. For each test, these conditions are reported in terms of dry bulb temperature T_{db} and absolute humidity ω, calculated according to Eq. (19), where the psychrometric approach is used and moist air is considered as a mixture of dry air and water vapor, both assumed to behave as ideal gases [35]. Finally, the different parameters were evaluated as a function of the *Re* for both the dry and wet channels.

$$\omega = 0.622\frac{p_{sat@T}RH_{\%}}{p_{atm} - p_{sat@T}RH_{\%}} \tag{19}$$

In all the tests, the water injection pump operated with a duty cycle of 2 s ON every 10 s, delivering a water flow rate of 109 g_{H2O}/min. Table 5 provides a comprehensive overview of the tested ranges for the gyroid-based IEC configurations, including inlet dry-bulb temperatures (T_1, T_2), absolute humidity (ω_1), and Re_{13}, Re_{24} for both channels.

3. Results

3.1. Characterization under dry conditions

The pressure drop across the tested HX was measured with an average uncertainty of 1.8 %, and its trend for each tested TPMS is shown in Fig. 4 as a function of *Re*, spanning both the transitional and turbulent flow regimes. The measurements are consistent with the experimental investigation by Reynolds et al. for a gyroid with $D_H = 4.5$ mm, whose pressure drop per unit of length are also included in the same figure.

The results for the friction factor are presented in Fig. 5, where a weak independence of f from *Re* is observed for $Re > 1000$ (clearly visible only for Gyr10 and Gyr7.5, where higher *Re* values were achieved). This suggests that the fully turbulent flow regime is established near this value, as previously reported in the literature [25].

The average uncertainty in the friction factor measurement is 8.2 %, primarily impacted by the volumetric flow rate uncertainty, which affects the calculation of the mean velocity. The use of the hydraulic diameter in the analysis appears reasonable, as the friction factor trends are consistent across the different geometries, converging to a common value of $f \approx 0.8$ for $Re > 1000$.

The evaluation of heat transfer in the absence of water evaporation was conducted through tests with similar Re numbers for both channels, varying the inlet air temperature difference (ΔT) between the two channels from 10 to 15 °C. In turbulent flow regimes, it has been demonstrated [26] that TPMS structures follow the generalized Dittus-Boelter equation ($Nu = aRe^b Pr^{0.4}$ [42]). Furthermore, the difference in inlet temperatures affects *Re* rather than *Pr*, which remains nearly constant at 0.67 for all tests. Assuming equal *Re* numbers in both channels, the conditions are thus considered comparable from the thermo-fluid dynamic point of view.

Table 5
Tests under wet conditions.

TPMS	$T_1[^\circ C]$	$\omega_1\left[g_{vap}/kg_{da}\right]$	$T_2[^\circ C]$	Re_{13}	Re_{24}
Gyr10	25 –50	9.4 –11.6	25 –50	1394 –2827	1541 –2963
Gyr7.5	30 –50	10.9 –12.7	30 –50	908 –1735	1054 –2061
Gyr5	27 –50	12.2 –15.7	27 –50	453 –969	508 –1020

The thermal conductivity of the plastic material (λ_{PLA}) was measured at 0.15 W/(m °C) with an estimated uncertainty of 9.3 %, using the method proposed by Dziob et al. [43]. This value falls within the range available for PLA in the Matweb database (https://www.matweb.com).

Fig. 6 shows the trends of the convective heat transfer coefficient (h) calculated under different test conditions, with an average measurement uncertainty of 9.7 %. The average uncertainty in *Re* is 4.1 %. As expected, h increases as the hydraulic diameter decreases and as *Re* rises, reaching maximum values close to 200 W/(m^2 °C) consistent with results reported by other authors.

Fig. 7 presents *Nu* calculated for the various gyroids tested, with an average measurement uncertainty of 9.8 %, along with the interpolating equation generated using the generalized Dittus-Boelter form: $Nu = 0.161Re^{0.8}Pr^{0.4}$ ($400 < Re < 2600$). This slightly differs from the equation determined by Reynolds et al. ($Nu = 0.49Re^{0.62}Pr^{0.4} \rightarrow 100 < Re < 2500$), whose results for gyroids in terms of *Nu* were obtained with $2 < D_H < 10mm$, represented by the dotted lines.

To contextualize the tests within the current body of literature, Fig. 8 compares the obtained *Nu* trends with results for other gyroid-based TPMS reported in previous studies.

The dry characterization of the HXs enables their behavior to be contextualized within the limited data currently available for these

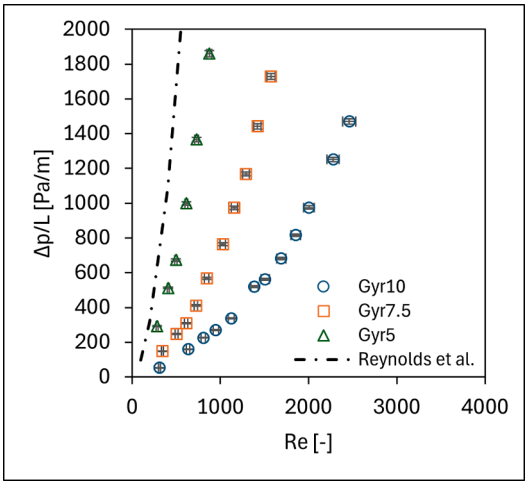

Fig. 4. Measured pressure drop per unit of length of the different gyroid-based HX across a range of ***Re***. A comparison with a gyroid HX with porosity of 37.5 % and hydraulic diameter of 4.5 mm from [26] is also reported.

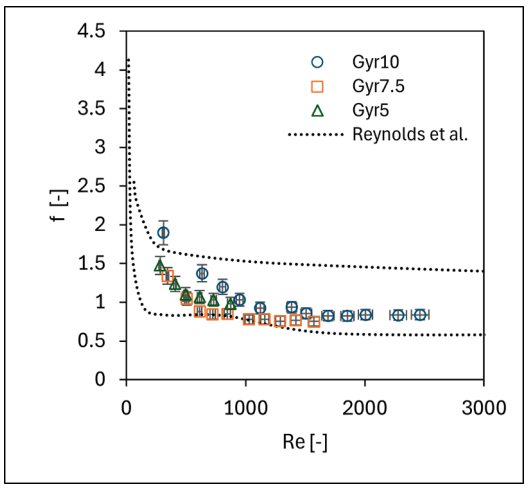

Fig. 5. Calculated values of the friction factor of the different gyroid-based HX across a range of ***Re***. A comparison with the lower and upper-band results obtained by Reynolds et al. for different D_h [26] is also reported.

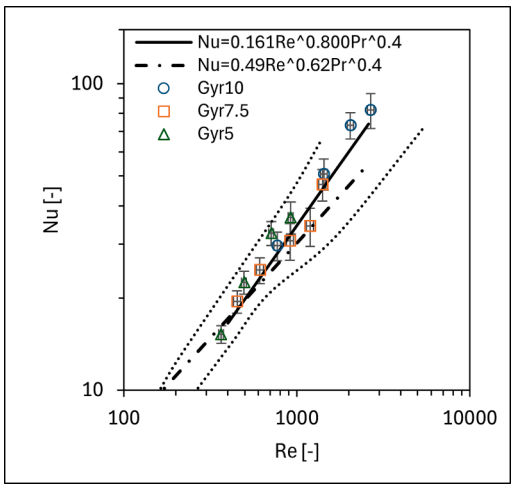

Fig. 7. Calculated ***Nu*** for the TPMS plotted along with the correlation found for this study. Dotted lines represent the upper and lower band of D_H for gyroids tested in [26].

geometries. However, it is important to point out that deriving universally applicable correlations remains challenging, as each seems to be framed to the specific geometry under study and the quality of the 3D printed parts. In fact, results are believed to be strongly affected by surface roughness, which depends not only on the type of printing technology but also on the specific 3D printer used [46,47].

This underscores the importance of thoroughly characterizing and contextualizing these HX under dry conditions before assessing their performance in indirect evaporative cooling applications. The next sections present the results obtained from testing gyroid-based exchangers for indirect evaporative cooling systems.

3.2. Characterization under wet conditions

The HX were tested under several inlet temperatures ($T_{1,2}$) and absolute humidity (ω) conditions, and with varying volumetric airflow rates through both the dry channel (1–3) and the wet channel (2–4), ranging from a minimum of 7.9 kg/h to a maximum of 28.7 kg/h depending on the pressure drop generated by the HX. The effect of airflow average velocity was assessed independently for the two channels: in the first set of tests, the airflow velocity in the wet channel (w_{24}) was kept constant while it was varied in the dry channel, and in the second set, the velocity in the dry channel (w_{13}) was held constant while it was varied in the wet channel.

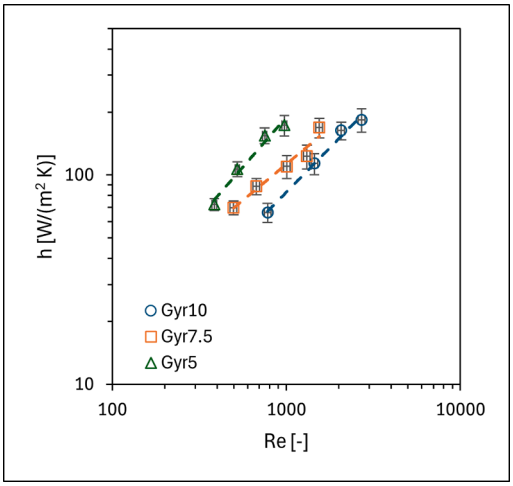

Fig. 6. Convective heat transfer coefficient for the different TPMS.

Fig. 9 shows the trends in cooling capacity under various operating conditions, where the figure legend indicates the type of HX used and the inlet air temperature conditions. The absolute humidity during the tests varied with environmental conditions and was measured as 14.6 g_{vap}/kg_{da} or Gyr5, 11.9 g_{vap}/kg_{da} for Gyr7.5, and 10.2 g_{vap}/kg_{da} for Gyr10. A discussion on the impact of absolute humidity variations is provided in the appendix.

w_{24} was set to an average of 2.0 m/s for Gyr5, 3 m/s for Gyr7.5, and 2.9 m/s for Gyr10, corresponding to *Re* of the wet channel equal to 739, 1535, and 2227, respectively. The average measurement uncertainty was 6.8 % for the cooling capacity ($\dot{Q}_{cool}$) and 5.8 % for the mean velocity w_{13} and w_{24}.

The graph shows a clear trend of increasing cooling capacity with higher volumetric airflow rates in the dry channel, which lead to an increase in the convective heat transfer coefficient, predominantly dependent on *Re* as demonstrated by the dry tests.

Even more sharp is the performance improvement with increasing inlet air temperature that can be explained by the steep decrease in relative humidity, which, in the wet channel, results in a higher vapor pressure gradient between the saturated air near the liquid film on the gyroid surface and air at the center of the channel. This directly correlates with the increase of the specific mass transfer coefficient, whose calculation depends on the local film temperature: a parameter that cannot be investigated with our experimental setup and would require dedicated CFD simulation.

It is also observed that the high absolute humidity reached during the Gyr5 tests leads to penalized performance, especially at lower temperatures (Gyr5@25 °C). It can therefore be concluded that Gyr5's performance could exceed the calculated values if adjusted to an absolute humidity level comparable to the other tests, which is not feasible with the current experimental setup, as it does not allow control over the inlet air absolute humidity.

These outputs raise the question of the role played by airflow velocity in the wet channel (w_{24}). Tests were therefore repeated, keeping the airflow velocity in the dry channel constant while varying the airflow rate in the wet channel. The cooling capacity was then calculated, and the results are presented in Fig. 10 where w_{13} was set to an average of 1.8 m/s for Gyr5, 2.4 m/s for Gyr7.5 and 2.6 m/s for Gyr10.

As expected, the cooling capacity shows a general little sensitivity to changes in velocity in the wet channel, resulting in no significant variations, often within the margin of measurement error.

However, different trends were observed in $\dot{Q}_{cool}$ of Gyr5 during

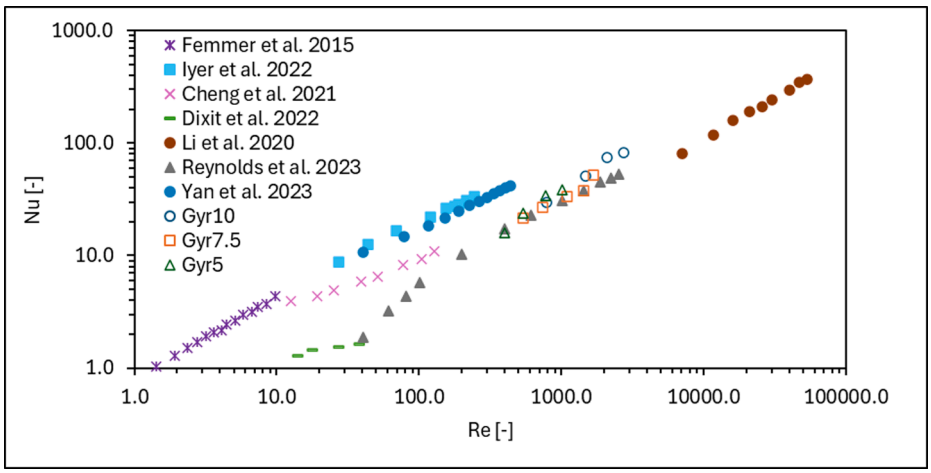

Fig. 8. Results of these tests compared with the results obtained by other authors on gyroids [21,26,27,30,31,44,45].

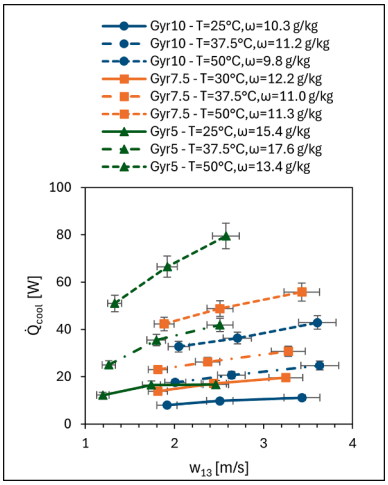

Fig. 9. Cooling capacity plotted over the dry channel average velocity at different $\boldsymbol{T}, \boldsymbol{\omega}$ inlet conditions and at constant flow rates in the wet channel.

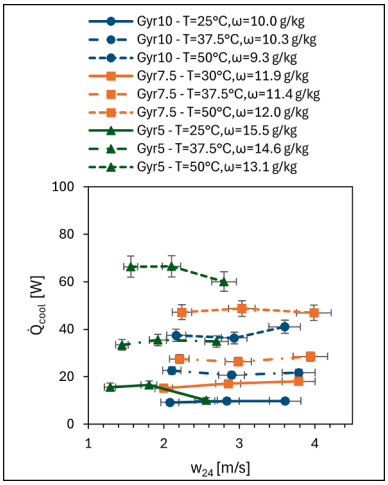

Fig. 10. Cooling capacity plotted over the wet channel average velocity at different $\boldsymbol{T}, \boldsymbol{\omega}$ inlet conditions and at constant flow rates in the dry channel.

testing. Specifically, a decrease in cooling capacity was recorded as the wet channel velocity increased, concurrently with a reduction in η_{wb}, as shown in Fig. 11.

The reduction in η_{wb} is consistent with findings reported by De Antonellis et al. [17] for conventional cross-flow HXs. In configurations where the inlet air temperatures of the wet and dry channels are similar (a condition comparable to our tests) an increase in the w_{24} can lead to this condition. This is due to the higher air temperatures in the wet channel, which may reduce the temperature drop achievable in the dry channel. The authors note that this effect can be mitigated by increasing the sprayed water flow rate to promote greater air saturation and, consequently, a more effective temperature reduction along the wet channel.

In the case of Gyr5 only, where the water flow rate was kept constant across all tests, it is hypothesized that a similar mechanism occurred but triggered by partial obstruction of the wet channel. It was observed that the narrower channel geometry of Gyr5, combined with the use of a nozzle producing large droplets (as in our setup), cause some parts of the HX to become partially blocked and excluded from airflow due to liquid accumulation.

Under these circumstances, preferential flow paths can develop, leading to locally increased airflow velocities compared to the average value measured and plotted. These preferential paths reduce the effective working surface of the HX, potentially limiting the overall performance of Gyr5.

The additional decrease in cooling capacity observed at higher w_{24} values (and not typical of crossflow HX as reported in Ref. [17]) is still attributed to the inhomogeneous water distribution that lead to a lower temperature drop in the dry channel airflow, which results in a lower η_{wb} compared to tests at low w_{24}.

This behaviour was not observed for Gyr7.5 (D_H = 8.5 mm) and Gyr10 (D_H = 12.6 mm), for which neither $\dot{Q}_{cool}$ nor η_{wb} show significant variation with changes in w_{24}. These observations and related hypotheses highlight the need for further dedicated experimental investigations on gyroid geometries with a hydraulic diameter below 8.5 mm. Future studies should specifically address the interaction between water flow characteristics, droplet size distribution, and surface wettability, as these factors may significantly affect channel wetting, flow distribution, and ultimately, the thermal performance of the HX.

The condition, generally verified, that wet channel velocity has limited impact on cooling capacity compared to changes in w_{13}, suggests technical optimization strategies for system operation. An initial evaluation is carried out through the assessment of the COP, which values are plotted from Figs. 12-14 as a function of the environmental conditions and velocities of the different channels, with an average measurement uncertainty on the calculated COP of 8.9 %. Each gyroid was tested at three different air velocities in the wet channel, while varying the air velocity in the dry channel. Fig. 12 shows the COP trends for low

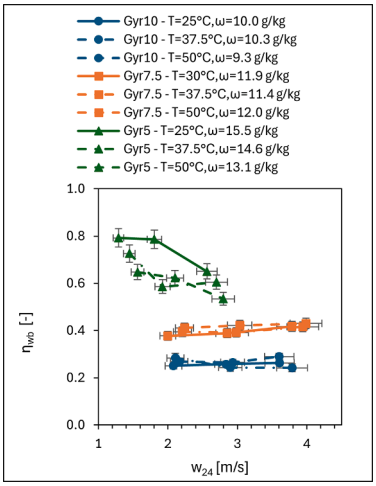

Fig. 11. Wet bulb efficiency plotted over the wet channel average velocity at different $\boldsymbol{T}, \boldsymbol{\omega}$ inlet conditions and at constant flow rates in the **dry** channel.

velocities in the wet channel (values are indicated in the caption), Fig. 13 refers to medium velocities, and Fig. 14 reports results for the highest tested velocities in the wet channel.

The COP value tends to decrease as the air velocity in the dry channel increases, with maximum COP values of 84.7, 57.9, and 59.3 recorded for Gyr5, Gyr7.5, and Gyr10, under conditions of $T = 50^{\circ}C$ and $RH_{\%}$ equal to 12.7 %, 14.7 %, and 17.1 % respectively. While the lowest COP values are observed under the maximum velocity conditions in the wet channel, as expected based on the results from Fig. 10, this is due to the additional pumping work required without registering any benefits in terms of cooling capacity.

The η_{wb} is reported from Figs. 15-17, following the same approach as in the previous figures. It is observed that η_{wb} is strongly influenced by the available HX surface area, with Gyr5 consistently exhibiting higher values compared to the other configurations, followed by Gyr7.5 and Gyr10. For Gyr5, it is important to consider that partial blockages in the wet channel (as already mentioned) may affect the results beyond the assumed margins of error. Nevertheless, the observed trends remain consistent and indexes of the potential performance of this geometry.

Confirming findings already available in the literature for traditional IECs [8,40], the η_{wb} decreases with increasing w_{13}, simply because the temperature difference (ΔT) in the dry channel becomes smaller due to the increased airflow which is not compensated by higher convective heat transfer coefficient. However (Fig. 16), the plots provide a clear positioning of the gyroid performance: η_{wb} ranges from 20 % to 33 % for Gyr10, from 31 % to 49 % for Gyr7.5, while Gyr5 shows a substantial improvement, with values between 47 % and 90 %, falling within the range typically expected for non-regenerative IECs.

In the case of an TPMS-based IEC, it is difficult to refer to prior art in the literature since, to the best of the authors' knowledge, no similar studies have been conducted so far. However, performance comparisons can be made with the limited studies available on IECs based on traditional crossflow hx with parallel aluminum channels, as done so far for the comparison of η_{wb} and referring once again to the findings presented in Ref. [17] and [11], which present results on the performance of different airflow configurations (counter-flow and parallel-flow) along with various water injection strategies and tests on different geometries for flat heat transfer surfaces. These studies were conducted on much larger HX compared to the TPMS-based devices in this work, with dimensions of 0.47 x 0.47 x 0.39 m in the Ref. [17] study and 0.7 x 0.7 x 0.2 m in the Ref. [11] and channel heights lower than 10 mm.

Similar geometries allow the full thermal development of the flow, differently for what is observed in TPMS geometries at the tested scales, where flow likely remains in a developing regime throughout the entire channel length.

In the first study, under operating conditions comparable to those tested in our work ($T_2 = 36.8^{\circ}C, \omega = 10.6 g_{vap}/kg_{da}, T_1 = 35^{\circ}C$) and air velocities in both channels of 3.7 m/s the achieved wet-bulb efficiency reached a maximum of 74 %, generating a temperature drop in the dry channel $\Delta T_{13} = 9.5^{\circ}C$ which leads to a cooling capacity of approximately 3800 W. When normalized to the HX volume, the volumetric cooling capacity is around 44 kW/m^3.

We can attempt to compare this result with our TPMS-based cases at $T_1 = T_2 = 37.5^{\circ}C$ for the Gyr10 and Gyr7.5 structures, which were tested at similar humidity levels and air velocities as those in De Antonellis's study and does not show the limitations of Gyr5. As shown in Fig. 18, the volumetric cooling capacities of Gyr7.5 operating in those conditions were respectively 107 kW/m^3 and 129 kW/m^3, as indicated by the data labels on the corresponding histogram bars. These values are 2.4–2.9 times higher; however, they should be properly contextualized in relation to the small size of the TPMS-based HXs employed, which do not meet predefined target outlet temperature requirements.

The high energy density achieved is attributed to the enhanced local convective heat transfer coefficient promoted by both the TPMS geometries and the not fully developed flow, which comes at the cost of a high-pressure drop for the fluid through the HX. For instance, Ref. [11] shows that their HX delivered a power density of 48.7 kW/m^3 (similar to Ref. [17]) with an operational COP of 32. This is calculated not considering water pumping costs and assuming an overall fan efficiency of 50 %, as in our study. The operating conditions in their study were $T_2 = 25^{\circ}C, \omega = 10 g_{vap}/kg_{da}, T_1 = 35^{\circ}C, w_{13} = 3.2 m/s$ and $w_{24} = 2.2 m/s$.

When comparing these results with our TPMS-based HXs under $T_1 = T_2 = 25^{\circ}C$ operating conditions, the COP for the Gyr10 structure results equal to 6.0 at 25 °C (increasing to 14.7 if $T_1 = T_2 = 37.5^{\circ}C$ conditions are considered). For the Gyr7.5 structure, the COP is 9.4 at 30 °C (25 °C sample point is not available) and 16.2 at 37.5 °C indicating a reduction by a factor of 2–5 compared to standard cross-flow HX.

Finally, we observe the data regarding the air outlet temperatures, recorded as a function of the inlet temperature while varying the air velocity in the dry channel. In Fig. 19, a maximum ΔT_{13} of 15.8 °C is observed, which occurs with the Gyr5 under the conditions of maximum inlet temperature (50 °C) and minimum relative humidity. The worst performance, on the other hand, occurs with an inlet temperature of 25 °C using the Gyr10 structure. In this case, ΔT_{13} is 1.8 °C. These data should be interpreted alongside the results in terms of η_{wb}: when η_{wb} is significantly below 1, this suggests that performance could certainly be improved by increasing the evaporation rate of the HX perhaps introducing porous or hydrophilic coatings. The PLA surface is, in fact, relatively hydrophobic, with a static water contact angle ranging from 75° to 85° [48], and its affinity for water varies depending on the surface finish of the printed material. In particular, for highly rough surfaces (often generated by a layer spacing of 0.3 mm or more) the contact angle can decrease to as low as 53° [49]. This further highlights how the results depend not only on the material itself but also on the print quality.

4. Conclusions

This study evaluated the thermo-fluid dynamic performance of indirect evaporative coolers based on gyroid geometries. The HXs were fabricated in PLA through FFF technology and designed in three different hydraulic diameters (Gyr5 = 6.1 mm, Gyr7.5 = 8.5 mm and Gyr10 = 12.6 mm) to explore the influence of cell size and surface-to-volume ratio on thermal performance.

In dry tests, the gyroid structures demonstrated high heat transfer capabilities, confirming the data reported in the literature, with maximum convective heat transfer coefficient reaching ≈ 170 W/(m^{2}K) for Gyr5 under turbulent flow conditions ($Re \approx 1000$). On the other side, the friction factor was confirmed to be a weak point of these geometries, stabilizing at $f \approx 0.8$ for $Re > 1000$ and leading to high pumping costs.

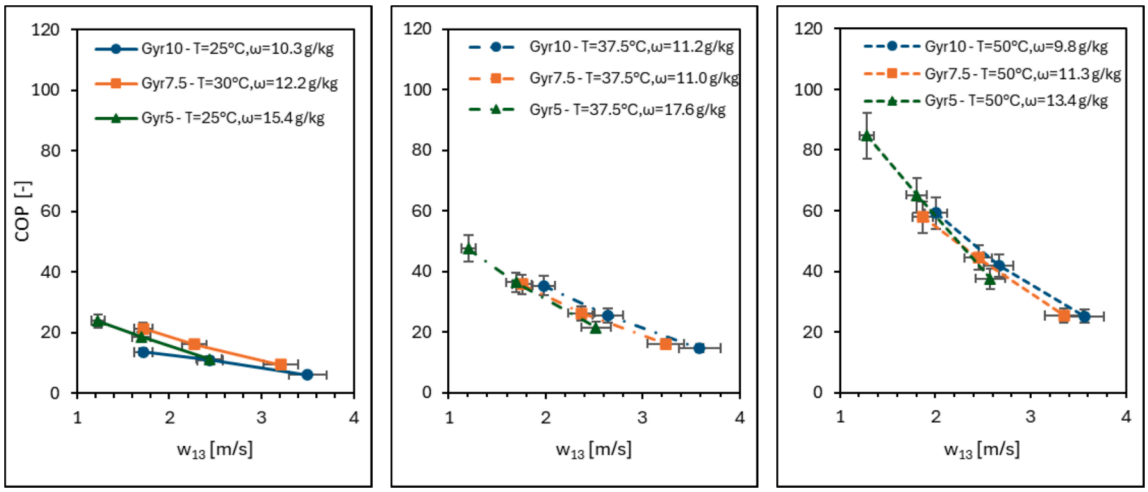

Fig. 12. Coefficient of performance plotted over the dry channel velocity at different $\boldsymbol{T}, \boldsymbol{\omega}$ inlet conditions. Wet channel velocity was kept constant at average values of 1.4 m/s for Gyr5, 2.2 m/s for Gyr7.5 and 2.1 m/s for Gyr10.

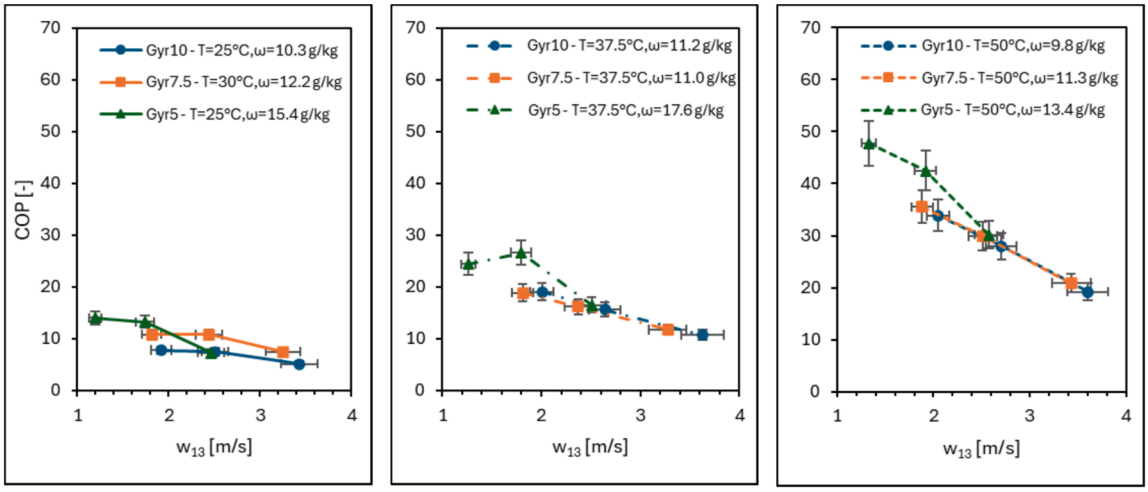

Fig. 13. Coefficient of performance plotted over the dry channel velocity at different $\boldsymbol{T}, \boldsymbol{\omega}$ inlet conditions. Wet channel velocity was kept constant at average values of 2.0 m/s for Gyr5, 3.0 m/s for Gyr7.5 and 2.9 m/s for Gyr10.

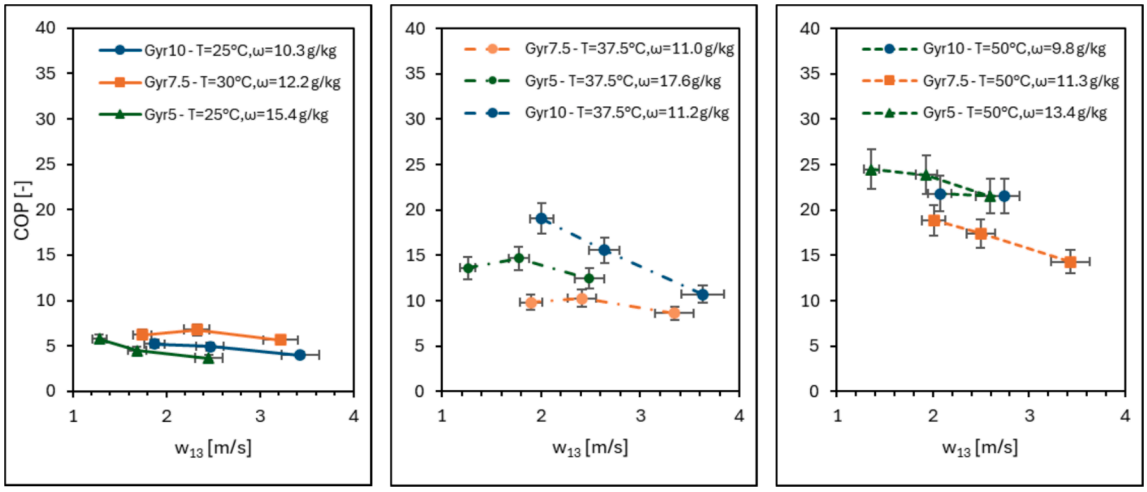

Fig. 14. Coefficient of performance plotted over the dry channel velocity at different $\boldsymbol{T}, \boldsymbol{\omega}$ inlet conditions. Wet channel velocity was kept constant at average values of 2.7 m/s for Gyr5, 3.9 m/s for Gyr7.5 and 3.7 m/s for Gyr10.

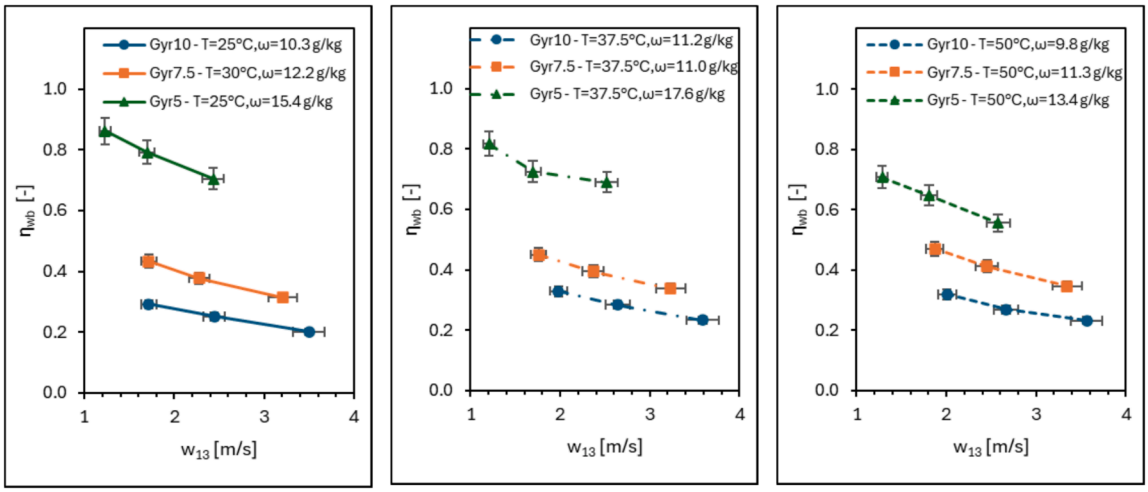

Fig. 15. Wet bulb efficiency plotted over the dry channel velocity at different $\boldsymbol{T}, \boldsymbol{\omega}$ inlet conditions. Wet channel velocity was kept constant at average values of 1.4 m/s for Gyr5, 2.2 m/s for Gyr7.5 and 2.1 m/s for Gyr10.

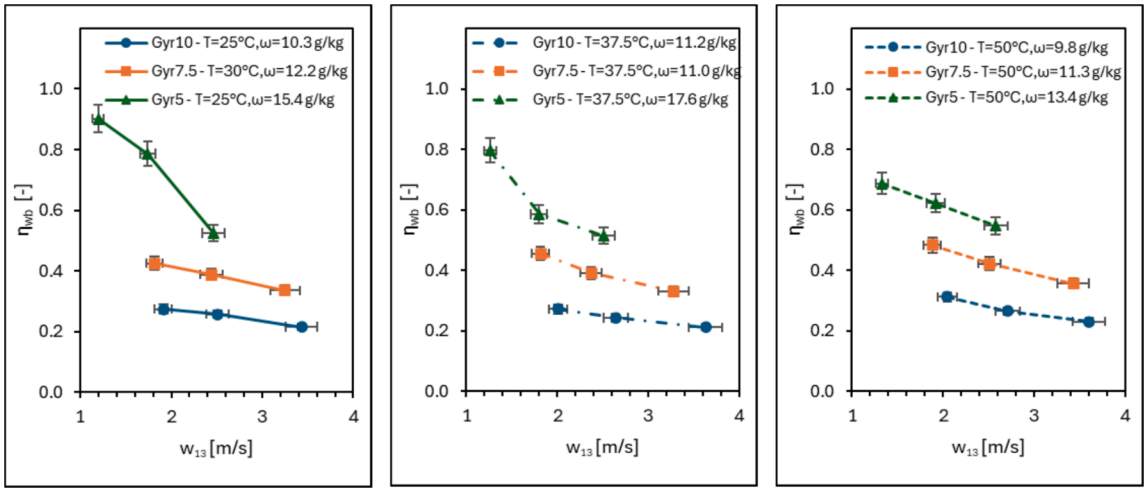

Fig. 16. Wet bulb efficiency plotted over the dry channel velocity at different $\boldsymbol{T}, \boldsymbol{\omega}$ inlet conditions. Wet channel velocity was kept constant at average values of 2.0 m/s for Gyr5, 3.0 m/s for Gyr7.5 and 2.9 m/s for Gyr10.

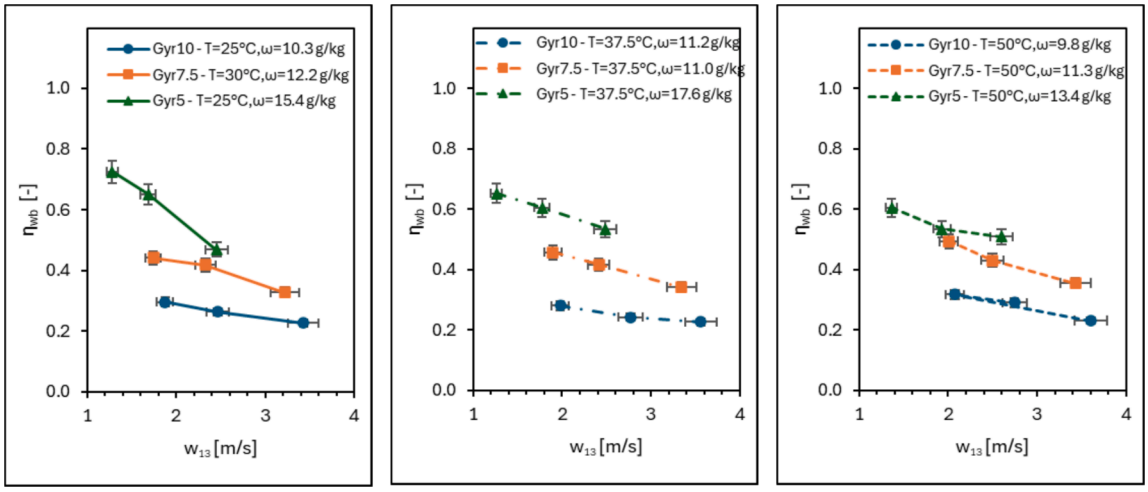

Fig. 17. Wet bulb efficiency plotted over the dry channel velocity at different $\boldsymbol{T}, \boldsymbol{\omega}$ inlet conditions. Wet channel velocity was kept constant at average values of 2.7 m/s for Gyr5, 3.9 m/s for Gyr7.5 and 3.7 m/s for Gyr10.

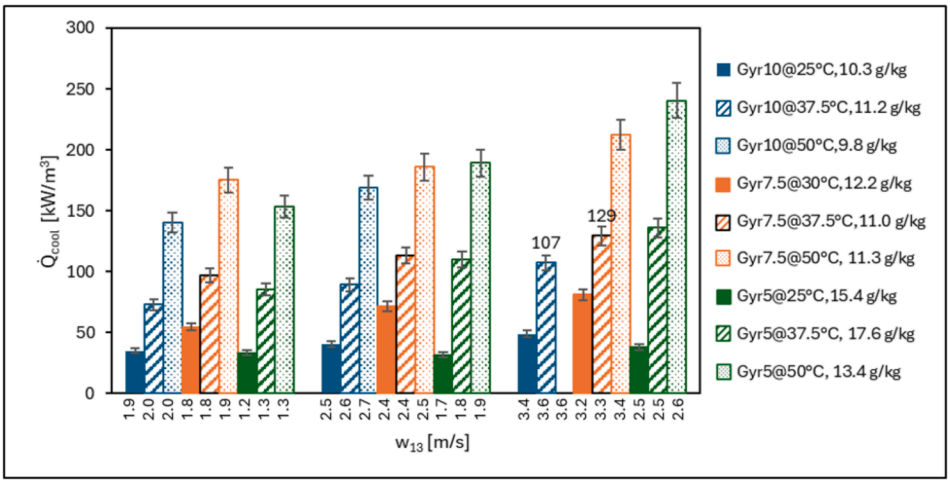

Fig. 18. Volumetric cooling capacity under different ambient air conditions with variable velocity in the dry channel shown on the x-axis. The average velocity in the wet channel is 2.7 m/s, 3.9 m/s and 3.7 m/s for Gyr5, Gyr7.5 and Gyr10 respectively. Labels are positioned on the values used for comparison with the literature.

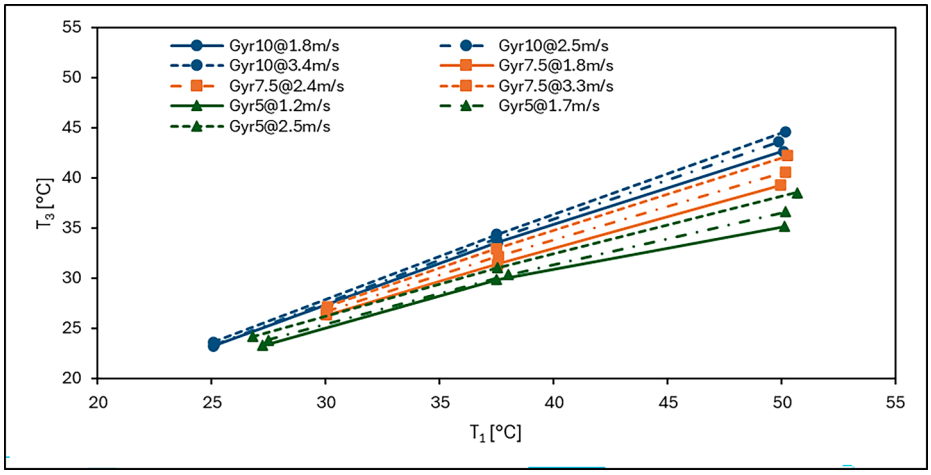

Fig. 19. Trend of the air outlet temperature from the dry channel (T_3) as a function of the inlet temperature (T_1) under different air velocity conditions in the dry channel reported in the legend.

Under wet conditions, the gyroid-based HX showed high performance as indirect evaporative coolers, achieving a volumetric cooling capacity that more than doubled the values typically obtained with crossflow plate HXs. For example, the Gyr7.5 achieved a volumetric cooling capacity of 129 kW/m^3 at an inlet temperature of 37.5 °C, significantly exceeding the 44 kW/m^3 reported for traditional aluminum HXs under comparable conditions. Nevertheless, it should be noted that smaller HXs often operate with higher temperature differences, which can lead to seemingly higher power density values. This aspect must be considered when comparing different technologies and represents a limitation of the present study.

The wet-bulb efficiency reached a maximum of 90 % for the Gyr5 highlighting the advantage of a high surface-to-volume ratio in promoting evaporation, while the COP achieved peak values of 84.7, 57.9, and 59.3 for the Gyr5, Gyr7.5, and Gyr10, respectively, under inlet temperatures of 50 °C and relative humidity ≈ 15 %. However, compared to standard cross-flow HXs operating under milder climate conditions the COP of TPMS-based results in a 2 to 5 times reduction.

These findings underscore the potential of gyroid geometries for applications where compactness is critical, although the elevated pressure drop remains a significant challenge for operational efficiency.

Future research should aim to optimize water distribution to both maintain high wet-bulb efficiency with larger hydraulic diameters and ensure uniform distribution in channels with hydraulic diameters below 8.5 mm. This includes applying surface coatings to the plastic structure to enhance evaporation rates and reduce the risk of clogging by promoting the development of a thin and continuous water film, exploring counterflow water nozzle configurations, and optimizing the timing of water spraying, ideally within full-scale HX prototypes to ensure scalability and practical applicability.

Declaration of competing interest

The authors declare that they have no known competing financial interests or personal relationships that could have appeared to influence the work reported in this paper.

Acknowledgements

This project was funded under the National Recovery and Resilience Plan (NRRP), Mission 4 Component 2 Investment 1.5 Call for tender No. 3277 of 30/12/2021 of the Italian Ministry of University and Research funded by the European Union NextGenerationEU. Project code ECS00000033, Concession Decree No. 1052 of 23/06/2022 adopted by the Italian Ministry of University and Research, No. CUP D93C22000460001, “Ecosystem for Sustainable Transition in Emilia-Romagna” (Ecosister), Spoke 4.

N.M. also acknowledges the financial support of the FAR

Dipartimentale 2023 program of the Dept. of Engineering 'Enzo Ferrari' - UniMORE for part of the instruments used in this study.

During the preparation of this work, the author(s) used Microsoft Copilot to improve the fluency and clarity of the English language. After using this tool, the author(s) reviewed and edited the content as needed and take full responsibility for the content of the publication.

Appendix A

A.1 Influence of absolute humidity on the results

The test rig used can control only the temperature, while the absolute humidity depends on environmental conditions. Although the tests were conducted under similar environmental conditions, some tests were repeated during a particularly humid day to evaluate the impact of humidity on the results. For the test conditions, it was decided to repeat the tests with the Gyr5 structure at an inlet temperature of 37.5 °C. The reference test, conducted with an absolute humidity of 12.0 g_{vap}/kg_{da}, was compared with a test condition at 17.6 g_{vap}/kg_{da}. As shown in Fig. A.1, the increase in ambient humidity reduces the cooling capacity of the indirect HX, leading to variations on the order of the measurement error. The same can be said for the coefficient of performance, while the wet bulb efficiency is the parameter most affected by the variation, since η_{wb} is calculated with reference to the wet bulb temperature, which itself is strongly affected by changes in absolute humidity.

For this reason, it is important to contextualize the results in terms of η_{wb} considering the environmental conditions used. To support this, the specific ambient conditions for each test have been explicitly reported in the figures throughout the article.

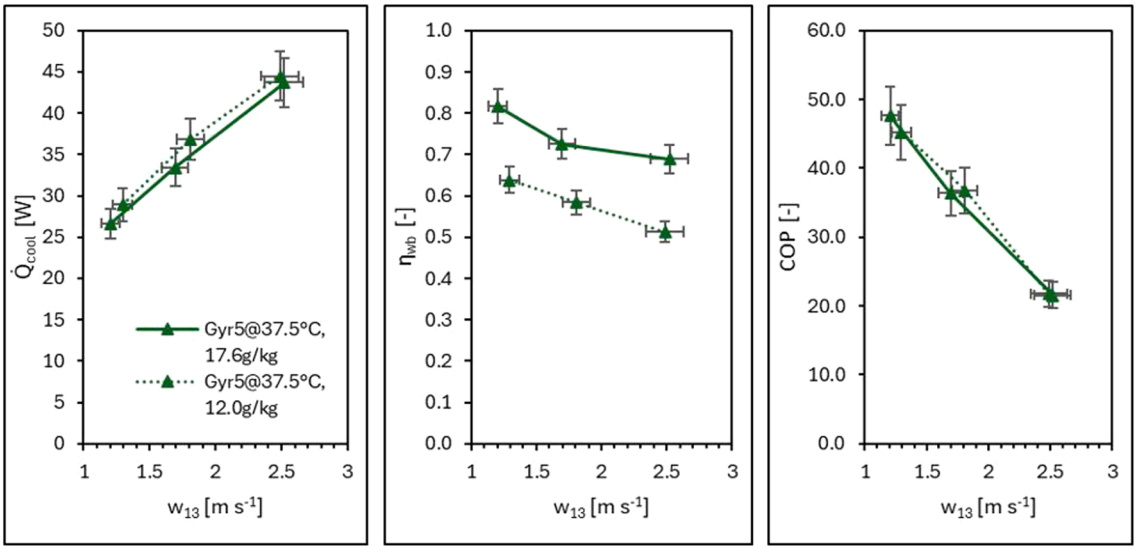

Fig. A.1. Comparison of cooling capacity (a), wet bulb efficiency (b), and coefficient of performance (c) for Gyr5 under different absolute humidity conditions.

Data availability

Data will be made available on request.

References

[1] M.A.D. Larsen, S. Petrović, A.M. Radoszynski, R. McKenna, O. Balyk, Climate change impacts on trends and extremes in future heating and cooling demands over Europe, *Energy Build* 226 (Nov. 2020) 110397, https://doi.org/10.1016/J.ENBUILD.2020.110397.

[2] International Energy Agency, "Space Cooling," 2023, *IEA, Paris*. [Online]. Available: https://www.iea.org/reports/space-cooling-2.

[3] International Energy Agency, "Space Cooling," 2022, *IEA, Paris*. [Online]. Available: https://www.iea.org/reports/space-cooling.

[4] Climate Central, "2022 Power Outages Report," 2022. [Online]. Available: file:///C:/Users/admin/Downloads/2022PowerOutages-1.pdf.

[5] European Commission, "A European Green Deal," 2020. [Online]. Available: https://ec.europa.eu/info/strategy/priorities-2019-2024/european-green-deal_en#actions.

[6] L. Gibbons, S. Javed, A review of HVAC solution-sets and energy performace of nearly zero-energy multi-story apartment buildings in Nordic climates by statistical analysis of environmental performance certificates and literature review, *Energy* 238 (Jan. 2022) 121709, https://doi.org/10.1016/J.ENERGY.2021.121709.

[7] H.S. Dizaji, E.J. Hu, L. Chen, S. Pourhedayat, Development and validation of an analytical model for perforated (multi-stage) regenerative M-cycle air cooler, Applied Energy 228 (2018) 2176–2194, https://doi.org/10.1016/J.APENERGY.2018.07.018.

[8] N. Kapilan, A.M. Isloor, S. Karinka, A comprehensive review on evaporative cooling systems, *Results Eng.* 18 (Jun. 2023) 101059, https://doi.org/10.1016/J.RINENG.2023.101059.

[9] H. Yang, W. Shi, Y. Chen, Y. Min, Research development of indirect evaporative cooling technology: An updated review, Renewable and Sustainable Energy Reviews 145 (2021) 111082, https://doi.org/10.1016/j.rser.2021.111082.

[10] E.V. Gómez, F.J.R. Martínez, F.V. Diez, M.J.M. Leyva, R.H. Martín, Description and experimental results of a semi-indirect ceramic evaporative cooler, *Int. J. Refrig* 28 (5) (2005) 654–662, https://doi.org/10.1016/j.ijrefrig.2005.01.004.

[11] S. De Antonellis, L. Cignatta, C. Facchini, P. Liberati, Effect of heat exchanger plates geometry on performance of an indirect evaporative cooling system, *Appl. Therm. Eng.* 173 (Jun. 2020), https://doi.org/10.1016/j.applthermaleng.2020.115200.

[12] J. Chu, W. Xu, Y. Fu, H. Huo, Experimental research on the cooling performance of a new regenerative dew point indirect evaporative cooler, *J. Build. Eng.* 43 (Nov. 2021), https://doi.org/10.1016/j.jobe.2021.102921.

[13] G. Zhu, W. Chen, S. Lu, Modelling of a dew-point effectiveness correlation for Maisotsenko cycle heat and mass exchanger, *Chem. Eng. Process. - Process Intesif.* 145 (Nov. 2019) 107655, https://doi.org/10.1016/J.CEP.2019.107655.

[14] Y. Min, Y. Chen, H. Yang, Numerical study on indirect evaporative coolers considering condensation: a thorough comparison between cross flow and counter flow, *Int. J. Heat Mass Transf.* 131 (Mar. 2019) 472–486, https://doi.org/10.1016/j.ijheatmasstransfer.2018.11.082.

[15] Seeley International, "Breezair TBSI 580 - Product Manual," 2024. [Online]. Available: https://www.seeleyinternational.com/eu/artefact/breezair-tbsi-580/.

[16] X. Zhao, S. Liu, S.B. Riffat, Comparative study of heat and mass exchanging materials for indirect evaporative cooling systems, *Build Environ* 43 (11) (Nov. 2008) 1902–1911, https://doi.org/10.1016/J.BUILDENV.2007.11.009.

[17] S. De Antonellis, C.M. Joppolo, P. Liberati, S. Milani, L. Molinaroli, Experimental analysis of a cross flow indirect evaporative cooling system, *Energy Build* 121 (Jun. 2016) 130–138, https://doi.org/10.1016/j.enbuild.2016.03.076.
[18] M.A. Jamil, et al., Experimental and parametric sensitivity analysis of a novel indirect evaporative cooler for greener cooling, *Therm. Sci. Eng. Prog.* 42 (Jul. 2023) 101887, https://doi.org/10.1016/J.TSEP.2023.101887.
[19] L. Zaheed, R.J.J. Jachuck, Review of polymer compact heat exchangers, with special emphasis on a polymer film unit, *Appl. Therm. Eng.* 24 (16) (2004) 2323–2358, https://doi.org/10.1016/j.applthermaleng.2004.03.018
[20] X. Chen, Y. Su, D. Reay, S. Riffat, Recent research developments in polymer heat exchangers–A review, Renewable and Sustainable Energy Reviews 60 (2016) 1367–1386, https://doi.org/10.1016/j.rser.2016.03.024.
[21] T. Dixit, E. Al-Hajri, M.C. Paul, P. Nithiarasu, S. Kumar, High performance, microarchitected, compact heat exchanger enabled by 3D printing, *Appl. Therm. Eng.* 210 (Jun. 2022), https://doi.org/10.1016/j.applthermaleng.2022.118339.
[22] S. Bardiya, J. Jerald, V. Satheeshkumar, Effect of process parameters on the impact strength of fused filament fabricated (FFF) polylactic acid (PLA) parts, *Mater Today Proc* 41 (2021) 1103–1106, https://doi.org/10.1016/j.matpr.2020.08.066.
[23] D.J. Whyte, R. Rajkhowa, B. Allardyce, A.Z. Kouzani, A review on the challenges of 3D printing of organic powders, *Bioprinting* 16 (2019) e00057, https://doi.org/10.1016/j.bprint.2019.e00057.
[24] M. Alteneiji, M.I.H. Ali, K.A. Khan, R.K.A. Al-Rub, Heat transfer effectiveness characteristics maps for additively manufactured TPMS compact heat exchangers, *Energy Storage Sav.* 1 (3) (Sep. 2022) 153–161, https://doi.org/10.1016/j.enss.2022.04.005.
[25] K. Dutkowski, M. Kruzel, K. Rokosz, Review of the state-of-the-art uses of minimal surfaces in heat transfer, Energies 15 (21) (2022) 7994, https://doi.org/10.3390/en15217994.
[26] B.W. Reynolds, C.J. Fee, K.R. Morison, D.J. Holland, Characterisation of heat transfer within 3D printed TPMS heat exchangers, *Int. J. Heat Mass Transf.* 212 (Sep. 2023), https://doi.org/10.1016/j.ijheatmasstransfer.2023.124264.
[27] J. Iyer, T. Moore, D. Nguyen, P. Roy, J. Stolaroff, Heat transfer and pressure drop characteristics of heat exchangers based on triply periodic minimal and periodic nodal surfaces, *Appl. Therm. Eng.* 209 (Jun. 2022), https://doi.org/10.1016/j.applthermaleng.2022.118192.
[28] S.D. Nath, S. Nilufar, An overview of additive manufacturing of polymers and associated composites, Polymers 12 (11) (2020) 2719, https://doi.org/10.3390/polym12112719.
[29] A. H. Schoen, "Infinite periodic minimal surfaces without self-intersections," May 1970.
[30] K. Yan, J. Wang, L. Li, H. Deng, Numerical investigation into thermo-hydraulic characteristics and mixing performance of triply periodic minimal surface-structured heat exchangers, *Appl. Therm. Eng.* 230 (Jul. 2023), https://doi.org/10.1016/j.applthermaleng.2023.120748.
[31] T. Femmer, A.J.C. Kuehne, M. Wessling, Estimation of the structure dependent performance of 3-D rapid prototyped membranes, *Chem. Eng. J.* 273 (Aug. 2015) 438–445, https://doi.org/10.1016/j.cej.2015.03.029.
[32] W. Li, W. Li, Z. Yu, Heat transfer enhancement of water-cooled triply periodic minimal surface heat exchangers, *Appl. Therm. Eng.* 217 (Nov. 2022), https://doi.org/10.1016/j.applthermaleng.2022.119198.
[33] T. M. Inc., "MATLAB version: 9.13.0 (R2022b)," 2022, *The MathWorks Inc., Natick, Massachusetts, United States*. [Online]. Available: https://www.mathworks.com.
[34] J. Riegel, W. Mayer, Y. van Havre, "FreeCAD (Version 0.16.6712)," 2017, *FreeCAD*. [Online]. Available: http://www.freecadweb.org.
[35] F.P. Incropera, D.P. DeWitt, *Fundamentals of Heat and Mass Transfer*, 4th Edition, John Wiley & Sons Inc, New York City, New York, 1996.
[36] A.M.S.J. Kline, The description of uncertainties in a single sample experiments, *Mech. Eng.* 75 (1953) 3–8.
[37] C. Qian, et al., Experimental investigation on heat transfer characteristics of copper heat exchangers based on triply periodic minimal surfaces (TPMS), *Int. Commun. Heat Mass Transfer* 152 (Mar. 2024), https://doi.org/10.1016/j.icheatmasstransfer.2024.107292.
[38] D. A. Reay, P. A. Kew, R. J. McGlen, "Heat transfer and fluid flow theory," Heat Pipes, pp. 15–64, Jan. 2014, https://doi.org/10.1016/B978-0-08-098266-3.00002-9.
[39] F. Wang, H. Jiang, Y. Chen, X. Li, Predicting thermal and mechanical performance of stochastic and architected foams, *Int. J. Heat Mass Transf.* 171 (Jun. 2021) 121139, https://doi.org/10.1016/J.IJHEATMASSTRANSFER.2021.121139.
[40] S. Moshari, G. Heidarinejad, A. Fathipour, Numerical investigation of wet-bulb effectiveness and water consumption in one-and two-stage indirect evaporative coolers, *Energy Convers. Manag.* 108 (Jan. 2016) 309–321, https://doi.org/10.1016/J.ENCONMAN.2015.11.022.
[41] R. Stull, Wet-bulb temperature from relative humidity and air temperature, *J. Appl. Meteorol. Climatol.* 50 (11) (2011) 2267–2269, https://doi.org/10.1175/JAMC-D-11-0143.1.
[42] Frank P. Incropera [and others]. *Fundamentals of Heat and Mass Transfer*. 6th ed., Hoboken, NJ: John Wiley, [2007] ©2007. [Online]. Available: https://search.library.wisc.edu/catalog/9910020981602121.
[43] S. Hughes, T. Croxford, D. Dziob, M. M. Mojcačepič, "Physics Education Simple method for measuring thermal conductivity Simple method for measuring thermal conductivity," 2020.
[44] Z. Cheng, X. Li, R. Xu, P. Jiang, Investigations on porous media customized by triply periodic minimal surface: heat transfer correlations and strength performance, *Int. Commun. Heat Mass Transfer* 129 (2021) 105713, https://doi.org/10.1016/J.ICHEATMASSTRANSFER.2021.105713.
[45] W. Li, G. Yu, Z. Yu, Bioinspired heat exchangers based on triply periodic minimal surfaces for supercritical CO_2 cycles, *Appl Therm Eng* 179 (2020) 115686, https://doi.org/10.1016/J.APPLTHERMALENG.2020.115686.
[46] A. Zimmer, J.D. PachecoAraújo, K.A. Andreassen, C.A. Grande, Effect of manufacturing techniques in pressure drop on triple periodical minimal surface packings, *Chem Ing Tech* 93 (6) (Jun. 2021) 967–973, https://doi.org/10.1002/cite.202000237.
[47] M.B. Hawken, S. Reid, D.A. Clarke, M. Watson, C.J. Fee, D.J. Holland, Characterization of pressure drop through Schwarz-Diamond triply periodic minimal surface porous media, *Chem. Eng. Sci.* 280 (2023) 119039, https://doi.org/10.1016/J.CES.2023.119039.
[48] E.H. Tümer, H.Y. Erbil, N. Akdoğan, Wetting of superhydrophobic polylactic acid micropillared patterns, *Langmuir* 38 (32) (Aug. 2022) 10052–10064, https://doi.org/10.1021/acs.langmuir.2c01708.
[49] N. Ayrilmis, Effect of layer thickness on surface properties of 3D printed materials produced from wood flour/PLA filament, *Polym. Test* 71 (Oct. 2018) 163–166, https://doi.org/10.1016/j.polymertesting.2018.09.009.